

# Topological Polar Textures in Freestanding Ultrathin Ferroelectric Oxides

Franco N. Di Rino<sup>1,\*</sup> and Tim Verhagen<sup>1,†</sup>

<sup>1</sup>*Institute of Physics, Czech Academy of Sciences,  
Na Slovance 2, 182 00, Prague 8, Czech Republic*

The remarkable advances achieved in two-dimensional materials are now being directly translated to low-dimensional oxides. Here we show using first-principles-based atomistic simulations that ultrathin freestanding ferroelectric layers host a rich variety of polar states, from liquid-like ferroelectric domains with long-range orientational order to helix-wave and chiral bubbles configurations reminiscent of those observed in twisted freestanding oxide layers. Time-dependent electric fields enable reversible control, revealing freestanding oxide layers as ideal platforms to explore complex polar states and their potential applications in future ferroic devices.

Ferroelectricity in low-dimensional systems favors the formation of a wide variety of topological structures, which emerge as an electrostatic mechanism to minimize the depolarizing energy associated with bound charges at the surfaces of uniformly polarized nanostructures [1–5]. These textures can be designed, stabilized, and reconfigured through confinement and boundary conditions, making their controlled manipulation appealing for future devices [6, 7]. Understanding how polarization adapts under spatial confinement is therefore essential to engineer topological states and advance nanoscale ferroelectric functionality.

Traditionally, the properties of ferroelectric thin layers have been tuned through substrate engineering, where epitaxial strain, mechanical clamping, and interfacial electrostatics dictate domain formation [8–12]. While these strategies have enabled remarkable progress, they constrain ferroic behavior to substrate-bound systems, where strong mechanical and electrical boundary conditions limit the material’s response.

Recent progress in two-dimensional (2D) materials has introduced powerful experimental routes to engineer functional properties via layer stacking. Interlayer degrees of freedom such as sliding, twisting, and reconstruction can break inversion symmetry and induce ferroelectric-like behavior [13–16]. Importantly, studies in the single-layer limit have revealed exceptionally rich physics spanning structural, electronic, and topological phenomena, as exemplified by graphene and related 2D van der Waals systems [17, 18]. These discoveries highlight how emergent behavior can arise even in the simplest, unconstrained geometries.

Inspired by these advances, similar design principles are now being extended to complex oxides, enabling the fabrication of freestanding and twisted oxide layers with atomic-level precision [19, 20]. For instance, Sánchez-Santolino et al. reported polarization vortex-antivortex arrays in twisted freestanding BaTiO<sub>3</sub> (BTO) layers [21], while related works have shown that such topological polarization textures can be tailored through twist and strain [22–24]. Although these developments bring oxide systems closer to the concepts explored in 2D materials,

research has so far focused mainly on complex stacked architectures, whereas the behavior of freestanding ultrathin oxides approaching the single-layer regime remains largely unexplored.

Freestanding ferroelectric layers thus provide an opportunity to examine polarization behavior in the absence of substrate-induced constraints. By removing external boundary effects, they provide a clean framework to explore the formation and stability of complex polarization textures in reduced dimensions. In this context, atomistic models parameterized from first-principles calculations offer a powerful tool to explore size effects, structural instabilities, dynamical behavior, and emergent polarization textures in low-dimensional, unconstrained environments. In this work, we employ a core-shell model to study the polarization patterns in freestanding BTO thin layers, revealing a variety of stable polar configurations (see End Matter for model and simulation details).

To elucidate how these patterns emerge and evolve, we systematically map the polarization configurations as a function of temperature and layer thickness  $N_z$ , defined as the number of Ti atoms along the pseudocubic  $z$  direction (Fig. 1). Starting from the paraelectric phase, we track the evolution of freestanding BTO layers of varying thicknesses upon cooling.

For ultrathin layers ( $N_z \leq 2$ ), no stable ferroelectric order develops, and the system remains dominated by thermal fluctuations.

For intermediate thicknesses ( $3 \leq N_z < 6$ ), temperature reduction stabilizes a single-domain *aa*-type ferroelectric phase, characterized by an in-plane polarization along the  $\langle 110 \rangle$  direction, while the out-of-plane component remains suppressed.

For thicker layers ( $N_z \geq 6$ ), the system instead organizes into three distinct nonuniform polar textures characterized by extended vortex textures.

Just below the paraelectric transition the system forms a *vortex-labyrinthine phase* [Fig. 2(a)], where alternating out-of-plane polarized domains arrange into an irregular, liquid-like labyrinth. Within this texture, the polarization rotates continuously across the mobile domain walls and defines vortex lines that fluctuate near the layer cen-

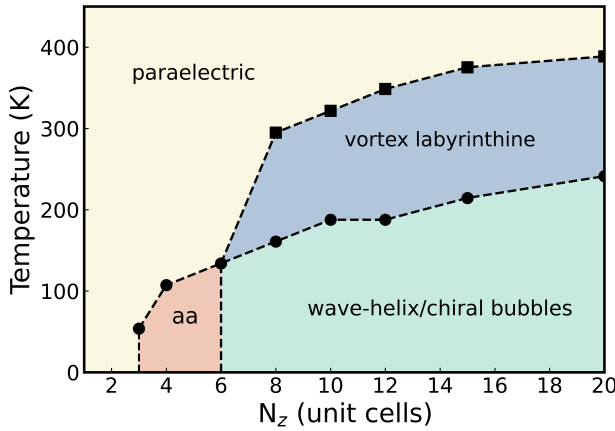


**FIG. 1:** Ferroelectric phases diagram (layer thickness  $N_z$  - temperature) in free standing BTO thin layers.

ter and occasionally bend into *Néel-type bubbles*. As a result, the labyrinthine texture progressively freezes. The vortex cores shift toward the layer surfaces, giving rise to two nearly degenerate low-temperature polar textures.

Upon further cooling, thermal fluctuations diminish and the labyrinthine texture progressively freezes. The vortex cores shift toward the layer surfaces, giving rise to two nearly degenerate low-temperature polar textures. The *wave-helix* state consists of elongated helical segments with a well-defined axis, producing stripe-like out-of-plane domains with a characteristic periodicity [Fig. 2(b)]. In contrast, the *chiral-bubbles* state develops square-like domains formed by bent helical cores that tend to close into toroidal loops, yielding bubble-like textures with a well-defined chirality [Fig. 2(c)].

Taken together, these temperature-driven transformations outline the phase diagram shown in Fig. 1, which closely resembles that obtained from thermodynamic free-energy calculations using the soft-domain analytical framework once surface-tension effects are included [29]. In that formulation, the polarization is represented through a small set of Fourier modes capturing the leading modulations, resulting in continuous textures where atomically sharp domain walls are not explicitly resolved. In both the analytical framework and our atomistic simulations, surface tension plays a central stabilizing role, strongly influencing the formation and persistence of modulated polar states. However, textures such as the chiral-bubble state lie beyond the scope of the minimal soft-domain description, as their stabilization requires additional energetic contributions and the superposition of multiple wavevectors.

Having established the phase diagram and identified the relevant polarization textures, we now provide a physical interpretation of the domain morphology and energetic balance of the two competing low-temperature

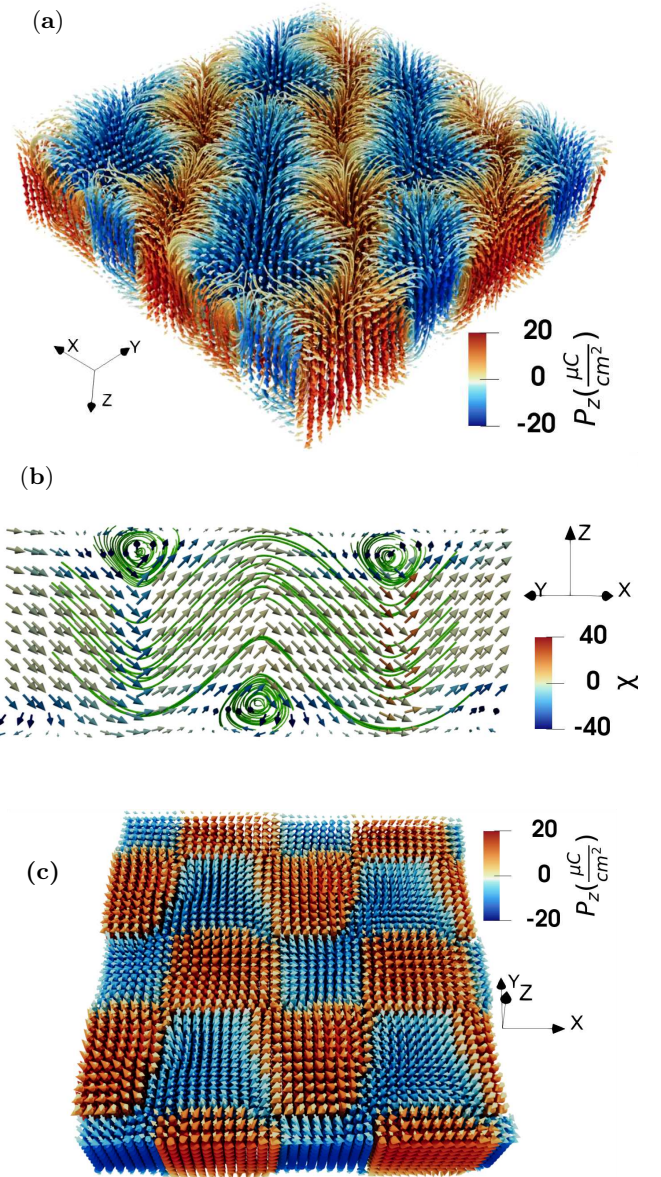


**FIG. 2:** Representative three-dimensional polarization textures stabilized at different temperatures in a freestanding BTO layer ( $N_z = 12$ ). (a) Vortex labyrinthine structure vector field. Streamlines serve as a guide to the eye (405 K). (b) Wave-helix (7 K). Cross-sectional view along a  $\langle 110 \rangle$  plane. Streamlines serve as a guide to eye. (c) Chiral-bubbles (7 K) vector field exhibiting square-like domain organization with alternating  $P_z$  orientation.

states.

In the wave-helix state [Fig. 2(b)], the in-plane polarization develops a dominant orientation along an equivalent  $\langle 110 \rangle$  direction, while the out-of-plane component modulates along the layer plane. This interplay produces stripe-like domains with a clear domain periodicity. The associated domain walls correspond to polarization rotations close to  $71^\circ$ , which are mechanically compatible with rhombohedral BTO [30]. While this stripe-domain

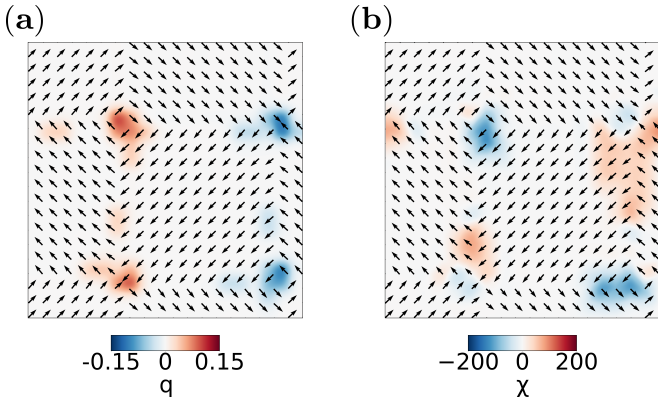


**FIG. 3:** Cross-sectional vector field view along a  $(001)$  plane.(a) Topological density charge  $q$  and (b) chirality density  $\chi$  map.

configuration minimizes the number of walls and preserves the full three-component polarization, it induces extended gradients of tetragonal distortion across the layer thickness.

By contrast, the chiral-bubble state [Fig. 2(c)] adopts a markedly different domain architecture. Here, the polarization forms square-like out-of-plane domains separated by sharp domain walls that cut across both pseudocubic in-plane directions. In three dimensions (3D), the polarization organizes into toroidal loops, where the helical cores periodically migrate between the two layer surfaces. This geometry preserves the helical character of the wave–helix state; however, instead of maintaining a well-defined axis, the cores bend and progressively tend to close into loops (see Fig. S1 in the Supplemental Material [31]). These patterns involve local polarization rotations corresponding to  $109^\circ$ ferroelectric domain walls, which are also compatible with rhombohedral symmetry [30]. Although a larger number of domain walls are introduced, they locally modulate the tetragonal strain and thereby relieve elastic stress without producing long-range gradients. Zero-temperature energy minimizations for a representative  $N_z = 12$  system identify the wave–helix as the ground state, although the energy difference with respect to the chiral-bubble configuration is marginal ( $\approx 0.3$  meV per formula unit). This near degeneracy reflects a delicate competition between distinct polarization textures and suggests that both configurations may be experimentally accessible depending on growth conditions or thermal history.

Among the stable low-temperature configurations, the chiral-bubble state stands out due to its intricate internal organization. To better elucidate its spatial arrangement, we consider suitable 2D projections of the polarization field. When projected onto the layer mid-plane, this configuration appears as an ordered array of alternating vortices and antivortices in the in-plane polarization components (Fig. 3). A similar vortex–antivortex

ordering has been reported in twisted ferroelectric layers [21], suggesting a common phenomenology emerging from modulated polarization fields. The corresponding topological charge density map, defined as  $q(x, y) = (1/4\pi)\mathbf{n} \cdot (\partial_x \mathbf{n} \times \partial_y \mathbf{n})$ , where  $\mathbf{n}$  is the normalized local polarization vector [32, 33], reveals a meron-antimeron arrangement resembling those reported in bulk configurations [Fig. 3 (a)] [34]. Complementarily, the chirality density map, given as  $\chi = \mathbf{P} \cdot (\nabla \times \mathbf{P})$  [5], reveals the topological handedness inherent to the individual helical cores, as visible in Fig. 3(b). As discussed by Luk'yanchuk *et al.* [5] for polar skyrmions in PTO/STO heterostructures [1], the Pontryagin index and the associated topological charge density characterize the topology within a given plane, but do not fully capture the intrinsically three-dimensional(3D) nature of chiral polarization textures. In our case, the computed topological charge represents a 2D projection of a fully 3D polarization field, whose magnitude and orientation vary across the layer thickness, as  $\mathbf{P}$  is not fixed. Together, the topological charge and chirality maps provide a complementary description of the chiral-bubble texture, capturing both its in-plane vortex–antivortex organization and the handedness of the underlying 3D polarization field.

While the preceding analysis highlights the mesoscopic topology of the polarization textures, it is also instructive to examine how these polarization patterns relate to the underlying local structural character of the layer. To this end, the local polarization was averaged over the simulation time and classified using a threshold-based criterion: unit cells were identified as rhombohedral when all 3D components exceeded  $7 \mu\text{C}/\text{cm}^2$ , orthorhombic when two components were dominant, tetragonal when a single component prevailed, and paraelectric when all components remained below  $7 \mu\text{C}/\text{cm}^2$ . The same threshold values were used for all layer thicknesses and were chosen conservatively so that all structural variants could be consistently identified.

This analysis reveals that freestanding BTO layers undergo a sequence of structural transformations that closely mirrors the bulk rhombohedral–orthorhombic–tetragonal–paraelectric phase transitions. At low temperatures, most cells exhibit three nonzero polarization components, consistent with a rhombohedral-like local character. Upon heating, one component progressively diminishes, giving rise to an orthorhombic-like regime within a narrow temperature window. With further temperature increase, the system evolves into a predominantly tetragonal-like configuration, and eventually into a weakly polarized, fluctuation-dominated paraelectric state (see Fig. S3 in the Supplemental Material [31]).

These results demonstrate that BTO, even under spatial confinement, preserves a sequence of structural transformations closely resembling those of the bulk. Confinement and finite-size effects modify the detailed polariza-

tion textures, yet the overall evolution of the average structure still follows the characteristic rhombohedral-orthorhombic-tetragonal-paraelectric progression. When initialized from wave-helix configurations, the simulations do not display a clearly developed orthorhombic phase. This could simply stem from the orthorhombic regime being restricted to a very narrow temperature interval in this model.

To connect these real-space polarization textures with their characteristic length scales, we next analyze the structure factor of the out-of-plane polarization component obtained from molecular dynamics simulations for a representative  $N_z = 12$  system.

This statistical measure, previously applied to PTO/STO superlattices [26], provides a sensitive probe of spatial correlations and domain morphology. Representative snapshots and schematic illustrations are shown in Fig. 4.

In the low-temperature regime, two distinct stable configurations can be identified. The first corresponds to a pinned stripe-like domain pattern [Fig. 4(a-b)], whose reciprocal-space signature consists of two sharp diagonal lobes in the structure factor at  $\mathbf{q} = (\mp\frac{1}{d}, \pm\frac{1}{d})$  u.c.<sup>-1</sup> (with  $d = 20$  being the domain periodicity), together with additional low-order harmonics. These secondary maxima originate from the diagonal domain orientation, which precludes a simple two-domain configuration and accommodates multiple domains within the simulation cell. This anisotropic scattering reflects a static twofold-symmetric arrangement of alternating out-of-plane polarizations oriented along the  $\langle 110 \rangle$  /  $\langle \bar{1}\bar{1}0 \rangle$  directions, although an equivalent variant with lobes along the opposite diagonals ( $\langle 1\bar{1}0 \rangle$  /  $\langle \bar{1}10 \rangle$ ) may also occur depending on the initial conditions or selected domain variant.

The second configuration, the chiral-bubble state [Fig. 4(c-d)], displays a structure factor with four well-defined rectangular lobes distributed along the diagonals at  $q_x = \pm 1/20$  and  $q_y = \pm 1/20$ . This pattern originates exclusively from the modulation of the out-of-plane polarization component  $P_z$ . The peak positions encode the periodicity and preferred orientation of the  $P_z$  variations, while the rectangular shape of the lobes reflects the in-plane anisotropy of the domains, which are slightly elongated along one direction.

Upon heating, both configurations evolve toward a common high-temperature regime [Fig. 4(e-f)], where the structure factor becomes more diffuse while retaining an approximate fourfold symmetry along equivalent  $\langle 110 \rangle$  directions. This behavior reflects the loss of long-range translational order while preserving orientational correlations, consistent with a liquid-like regime exhibiting tetratic orientational symmetry. Such fourfold orientational order, distinct from the sixfold symmetry characteristic of hexatic phases, reflects the influence of the underlying perovskite lattice and contrasts with the ordering reported in engineered ferroelectric heterostruc-

tures [26].

In real space, this regime is accompanied by enhanced domain dynamics, as polarization domains begin to meander, merge, and undergo coherent flips, giving rise to a fluctuating labyrinthine state. The emergence of this behavior in a single-component BTO layer evidences an intrinsic form of frustrated ferroelectric order. Although labyrinthine patterns lack translational order by construction, the observed phase demonstrates that these structures nonetheless retain a preferred orientational tendency. Comparable fourfold diffuse scattering has been reported in two-dimensional antiferromagnetic systems [35], where competing interactions give rise to melt-like orientational order.

At higher temperatures [Fig. 4(g-h)], the four lobes broaden and lose contrast, reflecting the progressive loss of spatial correlations and the emergence of an isotropic liquid-like behavior. In this regime, polarization fluctuations dominate, and the system evolves into a fully disordered state, marking the eventual loss of ferroic order.

It is worth noting that the nematic-like orientational dynamics are confined to the layer plane. No polarization mixing occurs across the layer thickness, as the out-of-plane polarization remains coherently aligned across the entire layer thickness due to strong electrostatic and elastic couplings.

Finally, we explore the possibility of switching between the two low-temperature topological states: the chiral-bubble state and the wave-helix state. Starting from the chiral-bubble configuration, a static or low-frequency electric field, sufficiently strong to break the closed topology ( $\approx 0.02V/\text{\AA}$  depending on thickness), aligns the polarization along a  $\langle 110 \rangle$  direction. This process drives the system into a wave-helix pattern, which remains robust upon field removal.

Achieving the reverse process, from the wave-helix back to the chiral-bubble state is more intricate. We demonstrate that time-dependent electric fields applied along  $\langle 110 \rangle$ , utilizing THz-frequency Gaussian pulses, can trigger a reorganization of the polarization field. This stimulus effectively transforms the stripe-like wave-helix morphology back into the chiral-bubble configuration.

For instance, in a  $N_z = 12$  system at 55 K, a Gaussian pulse  $E_0 e^{-(t-t_0/\tau)^2} \sin(\omega t)$  with frequency  $\omega = 5$  THz, amplitude  $E_0 = 0.01V/\text{\AA}$ , temporal center  $t_0 = 100$  ps, and pulse duration  $\tau = 40$  ps led to the formation of stable bubble domains after 240 ps of simulation. Comparable responses were obtained across different temperatures and initial states, indicating that the effect is robust.  $\omega$  and  $E_0$  influence the bubble size and in-plane rotation, while the pulse duration primarily determines the time required to pump the vibrational modes involved in the rotation dynamics.

This response may arise from anharmonic coupling between optical and acoustic modes. In bulk BTO, excitation of acoustic phonons can generate strain gradients

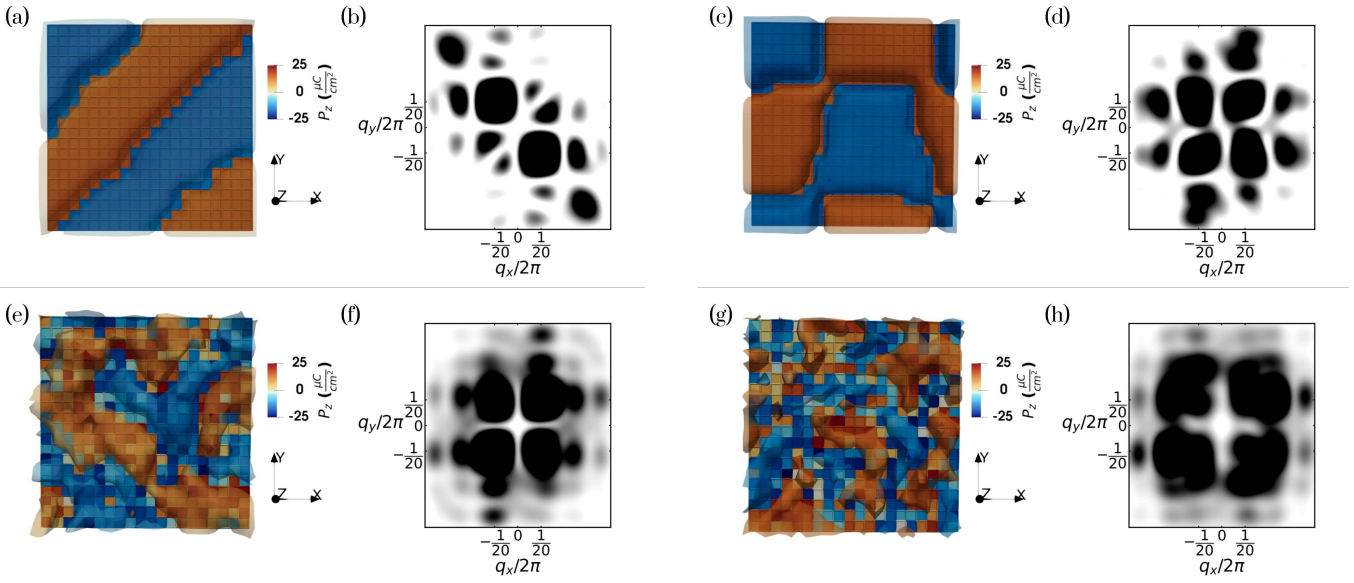


**FIG. 4:** Top-view snapshots of the out of plane polarization component ( $P_z$ ) of the layer. Panels (a), (c), (e), and (g) show instantaneous configurations at 7 K (stripe domain), 7 K (chiral-bubble domain), 300 K, and 325 K, respectively. The color lobes correspond to contour regions with similar  $P_z$  values. Panels (b), (d), (f), and (h) display the corresponding time averaged structure factors of the out-of-plane polarization component  $S(P_z)$

that stabilize vortex-antivortex structures [34]. In our confined layers, although the THz excitation primarily addresses optical phonons, the system behaves effectively as bulk-like within the plane, where near-degeneracy between optical and acoustic branches enhances the effect of symmetry-allowed coupling. Such anharmonic interactions could transiently reshape the local energy landscape, facilitating polarization rotations and the reorganization of toroidal structures.

Interestingly, this field-induced reorganization is not restricted to thicknesses where bubble states appear in equilibrium. Even ultrathin layers ( $3 \leq N_z < 6$  unit cells) in the in-plane *aa* phase can develop robust vortex-antivortex-like domains under analogous time-dependent fields. Unlike the bubble states in thicker layers, these flux-closure textures remain fully confined to the plane.

While the microscopic mechanism requires further clarification, these results point to nonlinear phononics as a potential pathway for dynamically engineering topological polarization states in confined ferroelectrics. Time-dependent electric fields therefore offer a viable route for manipulating, and potentially designing, topological states at the nanoscale.

Overall, our simulations show that freestanding BTO layers can sustain a wide range of topological polarization textures stabilized by electrostatic and elastic confinement. At low temperatures, two nearly degenerate states appear: a wave-helix phase and a chiral-bubble domain produced by helical cores that tend to close into loops. In 2D projections, these bubbles manifest as alternating vortex-antivortex pairs, consistent with recent observa-

tions in twisted freestanding BTO layers. As the system is heated, the in-plane polarization weakens and a vortex labyrinthine state emerges. Thermal fluctuations then drive a regime with tetratic symmetry, where positional order fades while orientational correlations persist over a finite temperature window. This behavior differs slightly from the squaric patterns reported in PTO/STO superlattices and resembles features seen in magnetic ultrathin layers. Finally, switching under time-dependent electric fields confirms that these low-temperature textures are not only stable but also responsive and controllable.

While our simulations capture several robust equilibrium configurations, other stable or metastable phases may still arise under conditions not examined here. In BTO, the extremely small energy differences between competing polar states make the system prone to hosting multiple nearly degenerate configurations, a hallmark of relaxor-like behavior. Understanding how such states appear and evolve under different external stimuli remains an important direction for future work.

A complementary analysis of the time-averaged local polarization shows that the system preserves the characteristic bulk-like rhombohedral-orthorhombic-tetragonal-paraelectric sequence under confinement, providing a structural counterpart to the topological transformations described above.

To conclude, these results highlight that even simple, freestanding ferroelectric layers exhibit a level of topological complexity and physical richness comparable to engineered heterostructures. Remarkably, such complexity arises without the lattice reconstruction or multilayer

design required in moiré systems, underscoring their potential as minimal yet powerful platforms for emergent ferroelectric polarization and topological phenomena.

## ACKNOWLEDGEMENT

We thank M. G. Stachiotti, M. Sepliarsky, P. Márton, M. Paściak, M. Graf, and M. A. P. Gonçalves for insightful discussions and constructive criticism. The authors acknowledge the financial support of the European Union by the ERC-STG project 2D-sandwich (Grant No 101040057) and the Operational Programme Johannes Amos Comenius of the Ministry of Education, Youth and Sport of the Czech Republic, within the frame of project Ferroic Multifunctionalities (FerrMion) [Project No. CZ.02.01.0100/22.0080004591], co-funded by the European Union. Computational resources were provided by the e-INFRA CZ project (ID:90254), supported by the Ministry of Education, Youth and Sports of the Czech Republic.

## END MATTER

### Simulation method

Molecular dynamics simulations were performed to investigate the polarization patterns and structural characteristics of freestanding BTO thin layers, using an interatomic potential derived from first-principles calculations [36, 37]. This framework has been extensively validated and has shown good agreement with experimental data, accurately reproducing the bulk properties of pure BTO, solid solutions, and mixed compounds [38–40]. The same theoretical scheme has also been applied to various low-dimensional BTO and PTO systems, including epitaxially strained thin layers and freestanding layers addressing surface energy effects [10, 29, 41, 42], which demonstrates the robustness and transferability of this approach. In this model, the relative displacement between the core and shell represents the ion's electronic polarization. Interatomic interactions include harmonic and fourth-order core-shell couplings ( $k_2$  and  $k_4$ ), long-range Coulomb forces, and short-range repulsive terms. Short-range interactions are modeled using two types of potentials: a Born-Mayer potential,  $V(r)=Ae^{-\frac{r}{\rho}}$ , for Ba-O and Ti-O, and a Buckingham potential,  $V(r)=Ae^{-\frac{r}{\rho}} + \frac{C}{r^6}$ , for O-O interactions, where  $r$  is the interatomic distance and  $A$ ,  $\rho$ , and  $C$  are model parameters.

The local polarization was defined as the dipole moment per unit volume of a perovskite unit cell, taken to be centered at the B-site cation and bounded by its nearest Ba neighbors. All atoms belonging to the conventional cell were included, and their instantaneous positions were

measured relative to the B-site reference position [43]:

$$\vec{p} = \frac{1}{v} \sum_i \frac{z_i}{w_i} (\vec{r}_i - \vec{r}_B), \quad (1)$$

where  $v$  is the unit-cell volume,  $z_i$  and  $\vec{r}_i$  are the charge and position of ion  $i$ , respectively, and  $\vec{r}_B$  denotes the position of the B-site atom. The factor  $w_i$  accounts for the number of unit cells shared by atom  $i$ .

The MD simulations were performed using the LAMMPS(23 June 2022) code [44] within a constant stress and temperature ( $N$ ,  $\sigma$ ,  $T$ ) ensemble, allowing relaxation of the in-plane stress components ( $\sigma_{xx}$ ,  $\sigma_{yy}$ ,  $\sigma_{xy}$ ), while keeping the out-of-plane components unconstrained to mimic a freestanding thin layer. Temperature and pressure were controlled using Nosé-Hoover thermostats and barostats, with a time step of 0.2 fs. The slabs were terminated with BaO planes on both surfaces, and periodic boundary conditions were imposed along the in-plane directions (x and y). The system was first equilibrated at 25 K and then heated to 405 K to reach the paraelectric phase. From this state, an annealing process was performed by cooling linearly at a rate of  $\approx 25$  K over 20 ps, followed by an additional 20 ps at constant temperature, during which structural and polarization data were collected. This annealing protocol was used to better sample stable configurations and avoid trapping the system in metastable states that can appear when simulations start directly from low temperatures.

Because the atomistic BTO model underestimates the bulk Curie temperature, all simulation temperatures were rescaled so that the effective  $T_c$  matches the experimental bulk value. This temperature adjustment is widely used in atomistic-model studies [27, 38, 41, 45]. Although the system studied here is not bulk, applying this correction provides a more meaningful reference scale and facilitates comparison with experimentally relevant temperature ranges.

To explore the stability of different phases, we considered cubic, tetragonal, orthorhombic and rhombohedral unit-cell starting configurations. To assess finite-size effects, we carried out simulations varying lateral dimensions and thicknesses at different temperatures. Thermal evolution and structural properties were then analyzed for each configuration.

Stress-free thin layers were modeled using simulation cells of size  $N_x \times N_y \times N_z$ , where  $N_i$  (with  $i = x, y, z$ ) denotes the number of Ti atoms along each pseudocubic direction.

We analyze systems with in-plane dimensions ranging from  $N_x = N_y = 15$  to 40 and thicknesses between  $N_z = 1$  to 20.

This systematic exploration of layers with different lateral sizes under periodic boundary conditions provides access to polarization configurations that represent simplified versions of those emerging in larger sys-

tems. At reduced scales, the system can stabilize a single, sometimes constrained, polarization state and allows the isolation of fundamental mechanisms. As the system size increases, these simple configurations evolve into more complex states involving multiple domains and dynamically interacting metastable structures. The size-dependent study therefore reveals how intricate polarization patterns emerge from basic structural units. Small systems expose the essential ingredients of collective behavior, whereas larger ones display emergent phenomena that arise only at extended scales. Identifying the stable configurations also provides valuable insight into the multiplicity of metastable states and lays the groundwork for understanding possible switching pathways between them.

To analyze the dynamics of the out-of-plane polarization, the instantaneous structure factor was calculated according [26]

$$S(q_x, q_y, q_z) = \left| \sum_{x=0}^{d-1} \sum_{y=0}^{d-1} e^{-i2\pi(xq_x+yq_y)} \bar{P}_z(x, y, z) \right|^2 \quad (2)$$

which corresponds to the Fourier transform of the out-of-plane polarization component  $\bar{P}_z(x, y, z)$  (x,y,z). We then average  $S(\mathbf{q})$  over the four central atomic planes and over time a 1600 ps simulation for each temperature.

---

\* dirino@fzu.cz  
 † verhagen@fzu.cz

[1] S. Das, Y. Tang, Z. Hong, M. Gonçalves, M. McCarter, C. Klewe, K. Nguyen, F. Gómez-Ortiz, P. Shafer, E. Arenholz, *et al.*, *Nature* **568**, 368 (2019).  
 [2] S. Das, Z. Hong, M. McCarter, P. Shafer, Y.-T. Shao, D. A. Muller, L. W. Martin, and R. Ramesh, *APL Mater.* **8**, 120902 (2020).  
 [3] Y.-T. Shao, S. Das, Z. Hong, R. Xu, S. Chandrika, F. Gómez-Ortiz, P. García-Fernández, L.-Q. Chen, H. Y. Hwang, J. Junquera, L. W. Martin, R. Ramesh, and D. A. Muller, *Nat. Commun.* **14**, 1355 (2023).  
 [4] J. Junquera, Y. Nahas, S. Prokhorenko, L. Bellaiche, J. Iñiguez, D. G. Schlom, L.-Q. Chen, S. Salahuddin, D. A. Muller, L. W. Martin, and R. Ramesh, *Rev. Mod. Phys.* **95**, 025001 (2023).  
 [5] I. A. Lukyanchuk, A. G. Razumnyaya, S. Kondovych, Y. A. Tikhonov, B. Khesin, and V. M. Vinokur, *Phys. Rep.* **1110**, 1 (2025).  
 [6] G. Catalan, J. Seidel, R. Ramesh, and J. F. Scott, *Rev. Mod. Phys.* **84**, 119 (2012).  
 [7] S. Chen, S. Yuan, Z. Hou, Y. Tang, J. Zhang, T. Wang, K. Li, W. Zhao, X. Liu, L. Chen, L. W. Martin, and Z. Chen, *Advanced Materials* **33**, 2000857 (2020).  
 [8] B.-K. Lai, I. Ponomareva, I. A. Kornev, L. Bellaiche, and G. Salamo, *Phys. Rev. B* **75**, 085412 (2007).  
 [9] K. M. Rabe, *Curr. Opin. Solid State Mater. Sci.* **9**, 122 (2005).  
 [10] S. Tinte and M. Stachiotti, *Phys. Rev. B* **64**, 235403 (2001).  
 [11] N. A. Pertsev, A. G. Zembilgotov, and A. K. Tagantsev, *Phys. Rev. Lett.* **80**, 1988 (1998).  
 [12] N. A. Pertsev, A. G. Zembilgotov, and A. K. Tagantsev, *Ferroelectrics* **223**, 79 (1999).  
 [13] M. Wu and J. Li, *Proc. Natl. Acad. Sci. U. S. A.* **118**, e2115703118 (2021).  
 [14] A. Weston, E. G. Castanon, V. Enaldiev, F. Ferreira, S. Bhattacharjee, S. Xu, H. Corte-León, Z. Wu, N. Clark, A. Summerfield, *et al.*, *Nat. Nanotechnol.* **17**, 390 (2022).  
 [15] Y. Hassan, B. Singh, M. Joe, B.-M. Son, T. D. Ngo, Y. Jang, S. Sett, A. Singha, R. Biswas, M. Bhakar, K. Watanabe, T. Taniguchi, V. Raghunathan, G. Sheet, Z. Lee, W. J. Yoo, P. K. Srivastava, and C. Lee, *Adv. Mater.* **36**, 2406290 (2024).  
 [16] S. Li, F. Wang, Y. Wang, J. Yang, X. Wang, X. Zhan, J. He, and Z. Wang, *Adv. Mater.* **36**, 2301472 (2024).  
 [17] K. S. Novoselov, A. K. Geim, S. V. Morozov, D. Jiang, Y. Zhang, S. V. Dubonos, I. V. Grigorieva, and A. A. Firsov, *Science* **306**, 666 (2004).  
 [18] A. H. Castro Neto, F. Guinea, N. M. Peres, K. S. Novoselov, and A. K. Geim, *Rev. Mod. Phys.* **81**, 109 (2009).  
 [19] A. Fernandez, M. Acharya, H.-G. Lee, J. Schimpf, Y. Jiang, D. Lou, Z. Tian, and L. W. Martin, *Adv. Mater.* **34**, 2108841 (2022).  
 [20] F. M. Chiabrera, S. Yun, Y. Li, R. T. Dahm, H. Zhang, C. K. R. Kirchert, D. V. Christensen, F. Trier, T. S. Jespersen, and N. Pryds, *Ann. Phys.* **534**, 2200084 (2022).  
 [21] G. Sánchez-Santolino, V. Rouco, S. Puebla, H. Aramburu, V. Zamora, M. Cabero, F. Cuellar, C. Munuera, F. Mompean, M. García-Hernandez, *et al.*, *Nature* **626**, 529 (2024).  
 [22] H. Sha, Y. Zhang, Y. Ma, W. Li, W. Yang, J. Cui, Q. Li, H. Huang, and R. Yu, *Nat. Commun.* **15**, 10915 (2024).  
 [23] C. Zhang, S. Zhang, P. Cui, and Z. Zhang, *Nano Lett.* **24**, 8664 (2024).  
 [24] S. Lee, D. J. P. de Sousa, B. Jalan, and T. Low, *Sci. Adv.* **10**, eadq0293 (2024).  
 [25] P. Zubko, J. C. Wojdel, M. Hadjimichael, S. Fernandez-Pena, A. Sené, I. Luk'yanchuk, J.-M. Triscone, and J. Iñiguez, *Nature* **534**, 524 (2016).  
 [26] F. Gómez-Ortiz, M. Graf, J. Junquera, J. Iñiguez-González, and H. Aramburu, *Phys. Rev. Lett.* **133**, 066801 (2024).  
 [27] Y. Nahas, S. Prokhorenko, Q. Zhang, V. Govinden, N. Valanoor, and L. Bellaiche, *Nat. Commun.* **11**, 5779 (2020).  
 [28] Y. Nahas, S. Prokhorenko, J. Fischer, B. Xu, C. Carrétéro, S. Prosandeev, M. Bibes, S. Fusil, B. Dkhil, V. Garcia, *et al.*, *Nature* **577**, 47 (2020).  
 [29] S. Kondovych, L. Boron, F. N. Di Rino, M. Sepliarsky, A. G. Razumnyaya, A. Sené, and I. A. Lukyanchuk, *Nano Lett.* **25**, 12987 (2025).  
 [30] P. Marton, I. Rychetsky, and J. Hlinka, *Phys. Rev. B* **81**, 144125 (2010).  
 [31] “See supplemental material at xxx for details about the topological analysis, temperature evolution and structural analysis, which includes refs. [5, 41, 47].” .  
 [32] Y. Nahas, S. Prokhorenko, L. Louis, Z. Gui, I. Kornev, and L. Bellaiche, *Nat. Commun.* **6**, 8542 (2015).  
 [33] M. A. P. Gonçalves, M. Paściak, and J. Hlinka, *Phys. Rev. Lett.* **133**, 066802 (2024).  
 [34] L. Bastogne, F. Gómez-Ortiz, S. Anand, and P. Ghosez, *Nano Lett.* **24**, 13783 (2024).

- [35] D. Abutbul and D. Podolsky, Phys. Rev. Lett. **128**, 255501 (2022).
- [36] M. Sepliarsky, A. Asthagiri, S. Phillpot, M. Stachiotti, and R. Migoni, Curr. Opin. Solid State Mater. Sci. **9**, 107 (2005).
- [37] P. Ghosez and J. Junquera, Annu. Rev. Condens. Matter Phys. **13**, 325 (2022).
- [38] R. Machado, Á. Di Loreto, A. Frattini, M. Sepliarsky, and M. Stachiotti, J. Alloys Compd. **809**, 151847 (2019).
- [39] M. Sepliarsky, R. Machado, S. Tinte, and M. G. Stachiotti, Phys. Rev. B **107**, 134102 (2023).
- [40] M. Sepliarsky, F. Aquistapace, F. Di Rino, R. Machado, and M. G. Stachiotti, Phys. Rev. B **112**, 214105 (2025).
- [41] M. G. Stachiotti and M. Sepliarsky, Phys. Rev. Lett. **106**, 137601 (2011).
- [42] F. Di Rino, L. Boron, M. A. Pavlenko, I. A. Tikhonov, A. G. Razumnaya, M. Sepliarsky, A. Sené, I. A. Lukyanchuk, and S. Kondovych, Commun. Mater. **6**, 57 (2025).
- [43] M. Sepliarsky and R. Cohen, Journal of Physics: Condensed Matter **23**, 435902 (2011).
- [44] A. P. Thompson, H. M. Aktulga, R. Berger, D. S. Bolineanu, W. M. Brown, P. S. Crozier, P. J. in 't Veld, A. Kohlmeyer, S. G. Moore, T. D. Nguyen, R. Shan, M. J. Stevens, J. Tranchida, C. Trott, and S. J. Plimpton, Comp. Phys. Comm. **271**, 108171 (2022).
- [45] J. Zhang, L. Bastogne, X. He, G. Tang, Y. Zhang, P. Ghosez, and J. Wang, Phys. Rev. B **108**, 134117 (2023).
- [46] J. Ahrens, B. Geveci, and C. Law, in *Visualization Handbook*, edited by C. R. Johnson and C. D. Hansen (Elsevier, 2005).

# Supplemental Material

## Topological Polar Textures in Freestanding Ultrathin Ferroelectric Oxides

Franco Di Rino<sup>1,\*</sup> and Tim Verhagen<sup>1,†</sup>

<sup>1</sup>*Institute of Physics, Czech Academy of Sciences,  
Na Slovance 2, 182 00, Prague 8, Czech Republic*

### TOPOLOGICAL ANALYSIS

To characterize the chiral bubble–domain structure, we computed the vorticity  $\omega$  of the polarization field  $\mathbf{P}$  [1],

$$\boldsymbol{\omega} = \nabla \times \mathbf{P}, \quad (1)$$

and identified helical cores by thresholding regions with large vorticity magnitude.

Streamlines were generated in ParaView [2] by interpolating the discrete polarization field, providing a qualitative visualization of how the polarization organizes into continuous toroidal loops. This representation highlights the three-dimensional arrangement of the helical cores, which periodically migrate between the top and bottom film surfaces. The analysis is intended as a qualitative tool to reveal the underlying topology rather than as a quantitative reconstruction of the vector field.

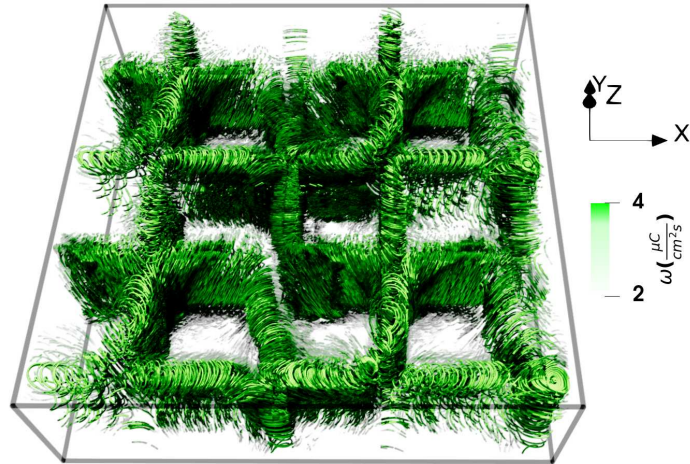


**FIG. S1:** Thresholded vorticity regions. Streamlines highlight the local polarization flow and reveal how the core axes gradually tilt and bend, eventually tending to close into loop-like structures.

### TEMPERATURE EVOLUTION

The temperature evolution of selected properties for a representative  $N_z = 4$  configuration is shown in Fig. S2. A similar qualitative behavior is observed for all systems with  $3 \leq N_z < 6$ . At low temperatures, the in-plane polarization dominates and persists up to approximately 135 K, where the polarization magnitude vanishes, as shown in Fig. S2(a). Above this temperature, the system progressively enters a paraelectric-like regime, with the net polarization of all three components approaching zero and becoming increasingly governed by thermal fluctuations. This temperature also marks a crossover in the lattice parameters [Fig. S2(b)], where the unit cells evolve from an orthorhombic-like to a tetragonal-like distortion. All quantities were obtained by averaging the polarization and lattice parameters over the entire simulation cell at each temperature.

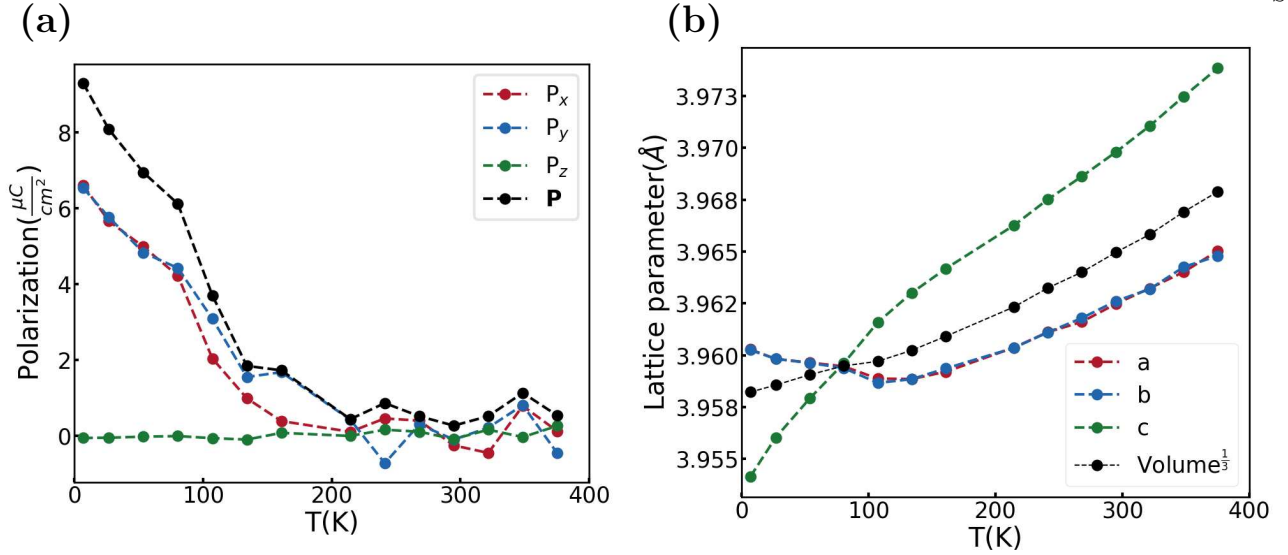


**FIG. S2:** Temperature dependence of the average squared polarization (a) and the average lattice parameters (b) of a configuration with  $N_z = 4$ .

### STRUCTURAL ANALYSIS

To complement the topological analysis in the main text, a simple polarization-based criterion is used to assign the local structural character of each unit cell throughout the simulations. The thresholds to distinguish different polarization orientations are chosen to give a clear and physically reasonable separation. Although more sophisticated schemes exist [3], this minimal approach is sufficient to capture the structural trends relevant here.

All simulated free-standing BTO layers with thickness  $N_z \geq 6$  display the same qualitative behavior discussed in the manuscript. Figure S3 shows the  $N_z = 12$  system as a representative example, illustrating how this polarization-based analysis complements the topological characterization of the emergent textures.

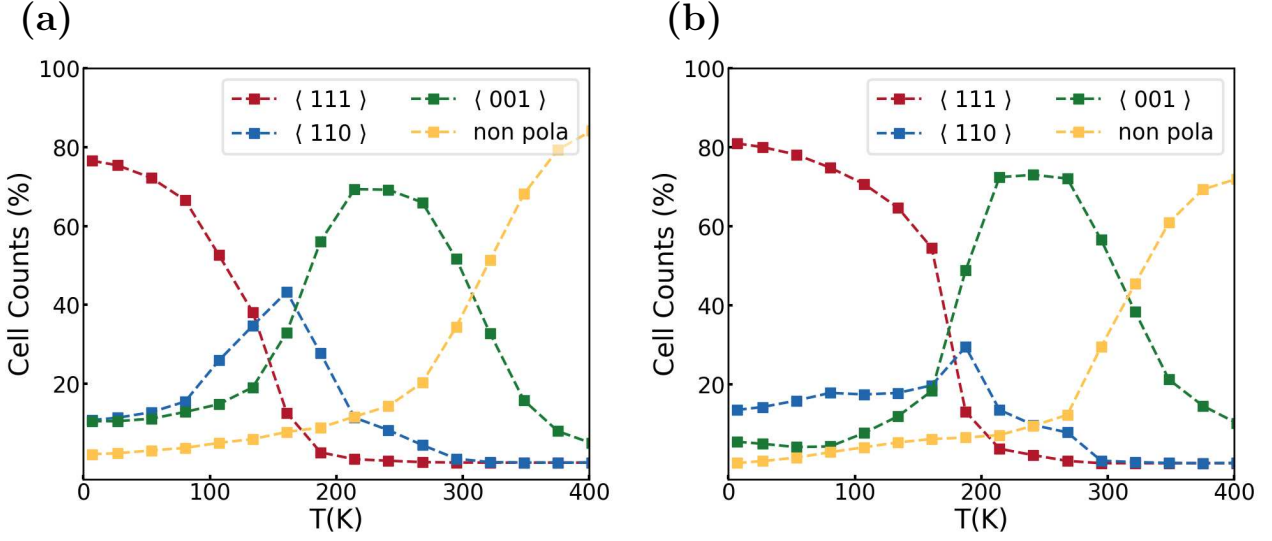


**FIG. S3:** Exemplary  $N_z = 12$  system structural evolution. (a) Starting from a chiral bubble state, the system follows the bulk-like rhombohedral-orthorhombic-tetragonal-paraelectric sequence under confinement. (b) Starting from wave-helix state, the orthorhombic phase does not clearly emerge.

\* dirino@fzu.cz

<sup>†</sup> verhagen@fzu.cz

- [1] I. A. Lukyanchuk, A. G. Razumnaya, S. Kondovych, Y. A. Tikhonov, B. Khesin, and V. M. Vinokur, Phys. Rep. **1110**, 1 (2025).
- [2] J. Ahrens, B. Geveci, and C. Law, in *Visualization Handbook*, edited by C. R. Johnson and C. D. Hansen (Elsevier, 2005).
- [3] M. Sepliarsky, F. Aquistapace, F. Di Rino, R. Machado, and M. G. Stachiotti, Phys. Rev. B **112**, 214105 (2025).